Soft Matter

Accepted Manuscript

ROYAL SOCIETY
OF **CHEMISTRY**

www.rsc.org/softmatter

Journal Name

ARTICLE TYPE

Cite this: DOI: 10.1039/xxxxxxxxxx

Received Date
Accepted Date

DOI: 10.1039/xxxxxxxxxx

www.rsc.org/journalname

Two types of Cassie-to-Wenzel wetting transitions on superhydrophobic surfaces during drop impact

Choongyeop Lee,*[a] Youngsuk Nam,*[a] Henri Lastakowski,[b‡] Janet I. Hur,[c] Seungwon Shin,[d] Anne-Laure Biance,[b¶] Christophe Pirat,[b] Chang-Jin "CJ" Kim,[c] and Christophe Ybert [b]

Despite the fact that superhydrophobic surfaces possess useful and unique properties, their practical application has remained limited by durability issues. Among those, the wetting transition, whereby a surface gets impregnated by the liquid and permanently loses its superhydrophobicity, certainly constitutes the most limiting aspect in many realistic conditions. In this study, we revisit this so-called Cassie-to-Wenzel transition (CWT) under the broadly encountered situation of liquid drop impact. Using model hydrophobic micropillars surfaces of various geometrical characteristics and high speed imaging, we identify that CWT can occur through different mechanisms, and at different impact stages. At early impact stages, right after contact, CWT occurs through the well established dynamic pressure scenario of which we provide here a fully quantitative description. Comparing the critical wetting pressure of surfaces and the theoretical pressure distribution inside the liquid drop, we provide not only the CWT threshold but also the hardly reported wetted area which directly affects the surface spoiling. At a latter stage, we report for the first time to our knowledge, a new CWT which occurs during the drop recoil toward bouncing. With the help of numerical simulations, we discuss the mechanism underlying this new transition and provide a simple model based on impulse conservation which successfully capture the transition threshold. By shedding light on the complex interaction between impacting water drops and surface structures, the present study will facilitate designing superhydrophobic surfaces with a desirable wetting state during drop impact.

1 Introduction

Inspired by non-adhesive plant leaves[1], superhydrophobic (SHPo)[2] surfaces – a hydrophobic surface decorated with micro- and/or nanoscale roughness – have attracted a lot of interest in recent years due to their unique and useful properties such as self-cleaning[3], anti-fouling[4,5], anti-icing[6] and drag reduction[7,8]. On the SHPo surfaces, water does not fill the void in between the surface roughness due to the capillary pressure, wetting only the uppermost region of the surface roughness and otherwise leaving an air layer underneath[9]. The reduced contact area between the liquid and the surface results in unusual static and dynamic behaviors of a water drop such as large contact angles and negligible contact angle hysteresis[9], as well as reduced friction and effective slippage of the liquid over the surface[7].

So far however, the usage of SHPo surfaces has been impaired by robustness and stability aspects. Aside resistance to wear or to chemical pollution, it is the possibility of superhydrophobicity loss through the Cassie-to-Wenzel wetting transition (CWT) which arguably constitutes the most limiting factor. In the Cassie state, the drop sits on the composite interface of solid and air patches, while in the Wenzel state, the drop homogeneously wets the micro/nanoscale roughness of the surface. Thus, the CWT is normally accompanied by a significant decrease of the drop mobility and the loss of the effective slip, which are unfavorable for most intended applications of SHPo surfaces. Note that it may be possible to revert to the Cassie state after the CWT occurs. But, doing so requires specially structured surfaces[10] or an external energy input[11,12]. The CWT can be triggered by various external means, such as drop squeezing[13], drop impact[14–17], vibration[18], and drop evaporation[19–22]. Among them, drop impact is the most

---

[a] Department of Mechanical Engineering, Kyung Hee University, Yongin 446-701, Korea. E-mail: cylee@khu.ac.kr, ysnam@khu.ac.kr
[b] Institut Lumière Matière, CNRS UMR 5306, Université de Lyon, Lyon, 69622 Villeurbanne Cedex, France.
[c] Mechanical and Aerospace Engineering Department, University of California, Los Angeles (UCLA), Los Angeles 90095, United States.
[d] Mechanical Engineering Department, Hongik University, Seoul, Korea.
‡Present address: Laboratoire de Physique de l'ENS de Lyon, CNRS UMR5672 and Université de Lyon, Lyon, France
¶Present address: University of Tokyo, Tokyo, Japan

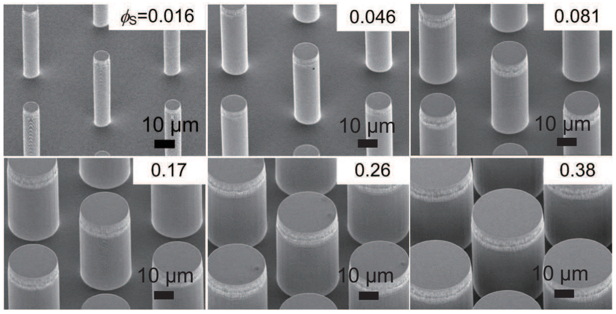

Fig. 1 Scanning electron microscope images of the micropillars with the fixed structural pitch $L = 50$ μm and height $H = 50$ μm and varying solid fraction ϕ_s.

common cause for the CWT on SHPo surfaces due to its relevance to many practical applications[23], and for this reason it is commonly employed to test or characterize the SHPo surface[24].

The present study focuses on the CWT induced by the impact of a water drop on a hydrophobic surface decorated with micropillars. After describing the experimental methods and numerical scheme, results are presented for the CWT as a function of surface properties and impact parameters. In the present study, two types of CWT are identified, depending on the impact velocities. If the impact velocity is high enough, the first type CWT appears right after the drop contacts the surface and corresponds to classically reported behavior. There, building on recent theoretical prediction for the development of dynamic pressure within the drop during the impact, measured thresholds for the first type CWT were shown to be in good quantitative agreement with a dynamics vs capillary imbibition criterion. Moreover, we report measurement of the hardly characterized wetted area and show that it can also be predicted following the same route. If however the impact velocity is not high enough to incur the first type CWT, we evidence a previously unknown second type CWT which occurs during the drop recoil. We discuss the mechanism underlying such phenomena with the help of numerical simulations and show that a simple model based on impulse conservation during the drop recoil and take-off describes the experimental observations of the second type CWT satisfactorily.

2 Materials and methods

2.1 Experimental methods

In the present study, a surface texture of cylindrical micropillars was patterned on a silicon substrate using photolithography followed by deep reactive ion etching (DRIE). First, a photoresist AZ5214 was spin-coated on 500 μm thick 4-in silicon wafer and was soft-baked at 95 °C. Then, the photoresist layer was exposed to UV light through a photomask and was subsequently developed and hard-baked at 120 °C. A silicon substrate was etched to the depth of 50 μm by DRIE process using the patterned photoresist layer as an etching mask. The remaining photoresist layer was removed using an oxygen plasma cleaner. Then, the whole surface was coated with a thin (a few nanometers thick) Teflon layer to make all the exposed surfaces hydrophobic.

Microscale pillars used in the current study were arranged in a square lattice with a fixed structural pitch L (center-to-center distance between two adjacent pillars) of 50 μm and varying top pillar area fractions (termed as a solid fraction throughout this study) ϕ_s defined as $\pi D^2/(4L^2)$ with D being a pillar diameter. The targeted ϕ_s was 0.02, 0.05, 0.1, 0.2, 0.3, and 0.4, but after fabrication the actual ϕ_s was measured to be 0.016, 0.046, 0.081, 0.17, 0.26, and 0.38, as shown in Fig. 1.

Drop impacts and CWTs were captured using a high speed camera (Photron SA-4) at up to 20,000 frames per second (fps). A water drop was released from a needle placed at different heights to obtain impact velocities U in the range between 0.1 and 3 m/s. Drop radius R_0 of 1.1 mm was used unless stated otherwise. Both side-view and top imaging have been performed depending on the targeted information: threshold of imbibition and extent of the wetting area, respectively.

2.2 Numerical methods

The droplet evolution during the impact was also investigated using a full 3D numerical model based on the level contour reconstruction method[25–27], a hybrid scheme that combines the advantage of the front tracking[28] and level set method[29]. In our model, a spherical water droplet of radius 1.1 mm is placed right above the bottom wall of the calculation domain (10 mm × 100 mm × 10 mm) with a downward impact velocity of U. The properties of water and air at 1 atm and 25 °C, typical ambient condition, have been chosen for the droplet and surrounding. It was shown that the droplet dynamics is strongly dependent on the surface condition in numerical simulation[26,27]. In our simulation, the advancing and receding angles are set in accordance to experiments to, respectively, 171° and 169° and incorporated to the developed model. At the superhydrophobic wall, we use the simple Navier-slip model that allows the contact line movement proportional to shear strain rate at the contact point. The contact line velocity U_{cl} is determined as $U_{cl} = \lambda \frac{\partial u}{\partial n}$ at the wall, where λ is an effective slip length. The effective slip length was estimated to be around 50 μm for $\phi_s = 0.05$ based on scaling law and exact calculations from previous numerical works[30–32].

3 Results and discussion

3.1 Two types of Cassie-to-Wenzel wetting transition

To study the CWT threshold for varying solid fraction ϕ_s and impact velocity U, side-view high speed imaging was chosen to precisely determine the wetting condition, as mentioned above. Indeed, Fig. 2b,c illustrate how proper lightening allows visualizing the air gap and pillar structure to determine whether and when water locally intrudes the surface. This direct observation led us to identify two distinct types of CWTs during drop impact. Fig. 2 exemplarily shows three scenarios of drop impact on a surface with nominal ϕ_s=0.05, two of the scenarios leading to wetting transition towards Wenzel states.

At high U of 0.64 m/s (Figure 2a), the CWT was induced immediately after contact between the water drop and the surface. This commonly known CWT was coined as type 1. At intermediate U of 0.48 m/s (Fig. 2b), despite no CWT occuring right after contact as in the previous case, a transition still exists but at a much

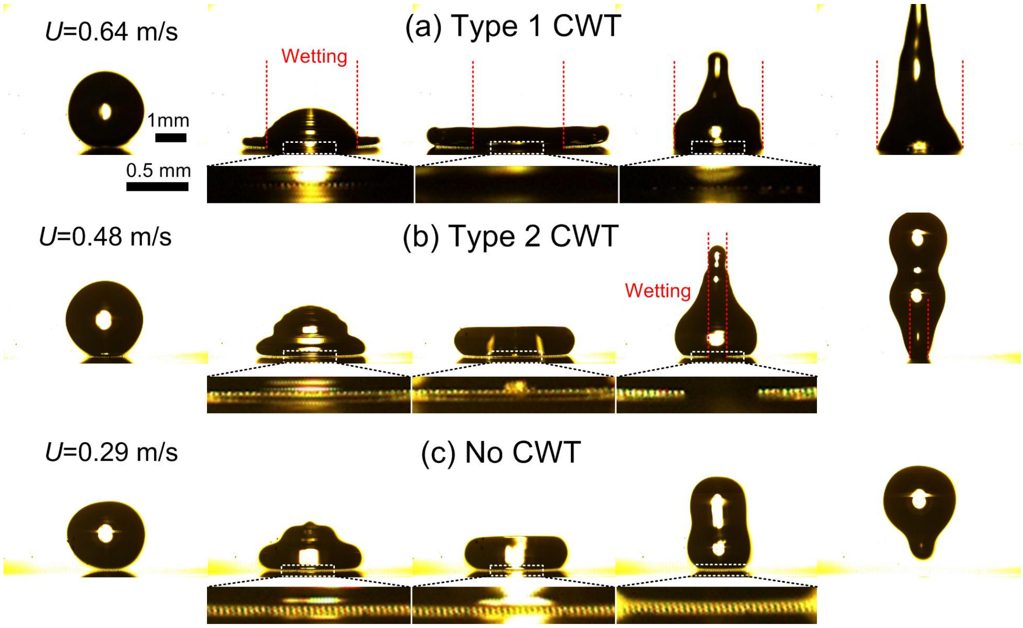

Fig. 2 Wetting transition upon drop impact on a SHPo surface of microscale pillars, shown for the case of nominal $\phi_s = 0.05$. (a) At U=0.64 m/s, type 1 CWT occurs during the initial contact, (b) At U=0.48 m/s, type 2 CWT occurs during the recoil, (c) At U=0.29 m/s, no CWT occurs. Enlarged images at the surface show the light passing through the dewetted region and blocked in the wetted region.

later time during recoil and prior to rebound. In addition, the rebounding drop appears pinned to the surface through a small and central wetted area. This CWT was coined as type 2. At low U of 0.29 m/s (Fig. 2c), a drop completely bounced off the surface without leaving any trapped water in between micropillars, as observed by unobtruded light penetration through micropillars during an entire drop impact process.

Focusing on the unexpected type 2 CWT, Fig.3 provides a sequence of drop images throughout the impact process, which allow to better identify the moment when the transition occurs. From contact up to the whole spreading stage, the light passing through the gap between the drop and the surface remains unchanged, confirming no transition during the initial vertical momentum transfer, as would classically occurs. Rather, the change in light transmission associated with liquid bridging across the air-gap clearly manifests during the recoil stage, right before a thin liquid jet is generated in the upper part of the drop. After a transient period lasting for 0.5-0.6 ms, and presumably due to meniscus changes or complex imbibition sequence, the clear image of a central wetted area is seen through complete blockage of light transmission. No further change is evidenced afterwards.

Overall, Fig.4a summarizes a Cassie-to-Wenzel wetting transition phase diagram identifying the different final wetted states as a function of impact velocity U and solid fraction ϕ_s (actual ϕ_s used). As an expected rule, the more robust the surface (large ϕ_s) the higher the required velocity U to induce wetting. However while the uppermost limit between squares and circle symbols materializes the familiar type 1 CWT, a new region appears in the lower-left region of the diagram corresponding to small solid fractions ϕ_s (here $\phi_s < 0.05$). This region corresponds to intermediate velocities, for which the wetting transition does occur, but through the new type 2 mechanism; with classical type 1 transition recovered only for large U.

To rationalize these findings, we first recall the origin of CWT: when the liquid pressure exceeds a critical capillary pressure, the solid-liquid-air contact line is depinned from the pillars' top edges, leading to the wetting transition[14,22]. On our cylindrical micropillars, the critical capillary pressure P_c (or maximum anti-wetting pressure), above which the contact line is depinned and CWT starts corresponds to the maximum pressure which the surface tension sustains. The wetting force acting on the surface per unit cell area L^2 is given as $P_c L^2(1-\phi_s)$, while the sustainable force by the surface tension is given as the product of the vertical component of surface tension $-\gamma\cos\theta_a$ and the perimeter of the liquid-solid contact line πD, where γ and θ_a are the surface tension of water (72 mN/m) and advancing CA on the smooth Teflon surface (120°), respectively. If D is expressed as a function of L and ϕ_s ($D = \sqrt{4L^2\phi_s/\pi}$), we can obtain the critical pressure P_c given by $P_c = -\frac{2\sqrt{\pi\phi_s}\gamma\cos\theta_a}{L(1-\phi_s)}$ [7,14]. The pillars used in the present study are made as tall as the pitch, so we expect that there is no premature CWT incurred by a deformed liquid-air interface contacting the basal region between the pillars before the contact line is depinned[14,22].

Now, the existence of two different types of CWTs in the present study suggests that two different mechanisms can contribute to liquid pressure build-up during the drop impact process. To help identifying these mechanisms, we used numerical simulations to visualize liquid pressure field throughout the drop impact dynamics on SHPo surfaces, under similar conditions with experiments. Fig. 5 shows the simulated drop impact behavior on SHPo surface, when the drop collides onto the surface with U=0.4 m/s. In Fig. 5a, a qualitative similarity of drop morphology with the experiment is clearly observed. Moreover, the pressure contour in Fig. 5b indicates the presence of two pressure peaks in the surface

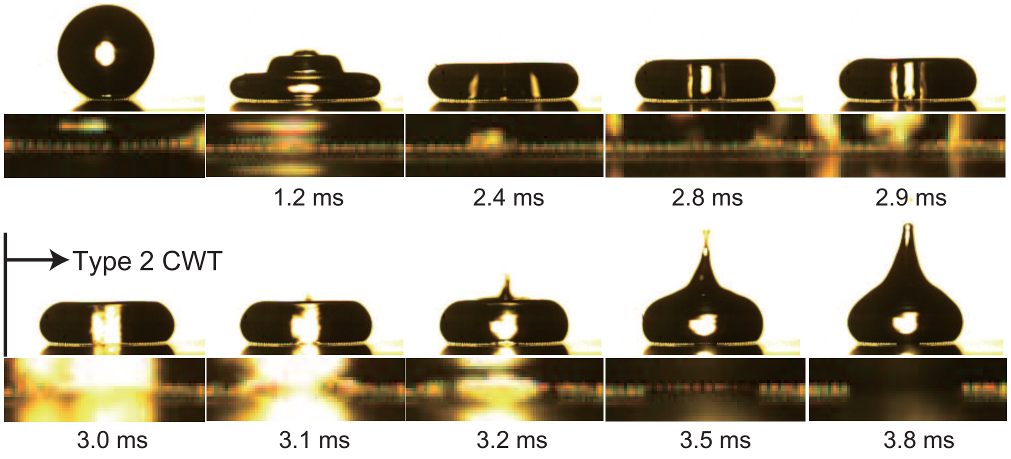

Fig. 3 Type 2 CWT observed on microscale pillars with target ϕ_s=0.05 at U=0.48 m/s. It is seen that the CWT occurs when the drop recoils from the surface.

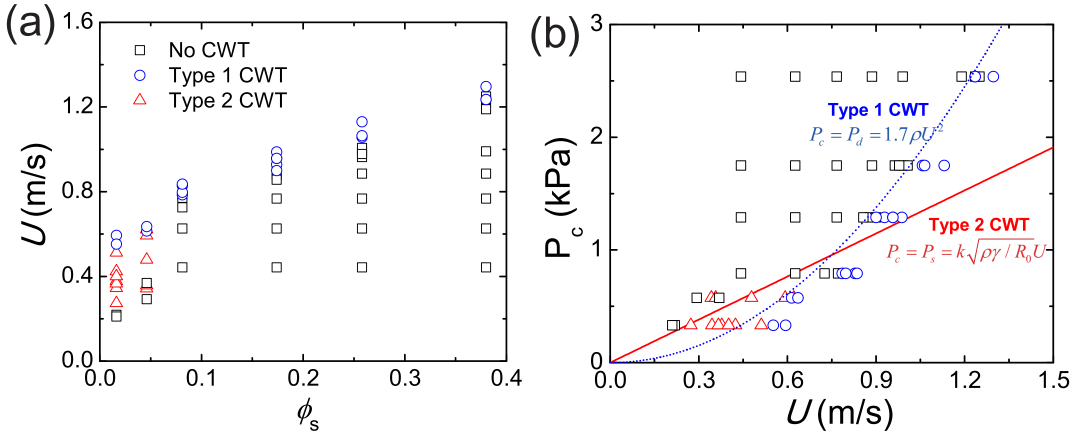

Fig. 4 (a) Three different wetting states observed on micropillars as a function of U and ϕ_s. ○: Type 1 CWT, △: Type 2 CWT, □: No CWT. (b) Theoretical CWT criteria of type 1 and type 2 are drawn by equilibriating $P_c = -\frac{2\sqrt{\pi\phi_s}\gamma\cos\theta_a}{L(1-\phi_s)}$ with two different wetting pressures: $P_c = P_d = 1.7\rho U^2$ (…) and $P_c = P_s = k\sqrt{\rho\gamma/R}U$ (–), respectively. The two observed CWT criteria agree with the two theoretical criteria.

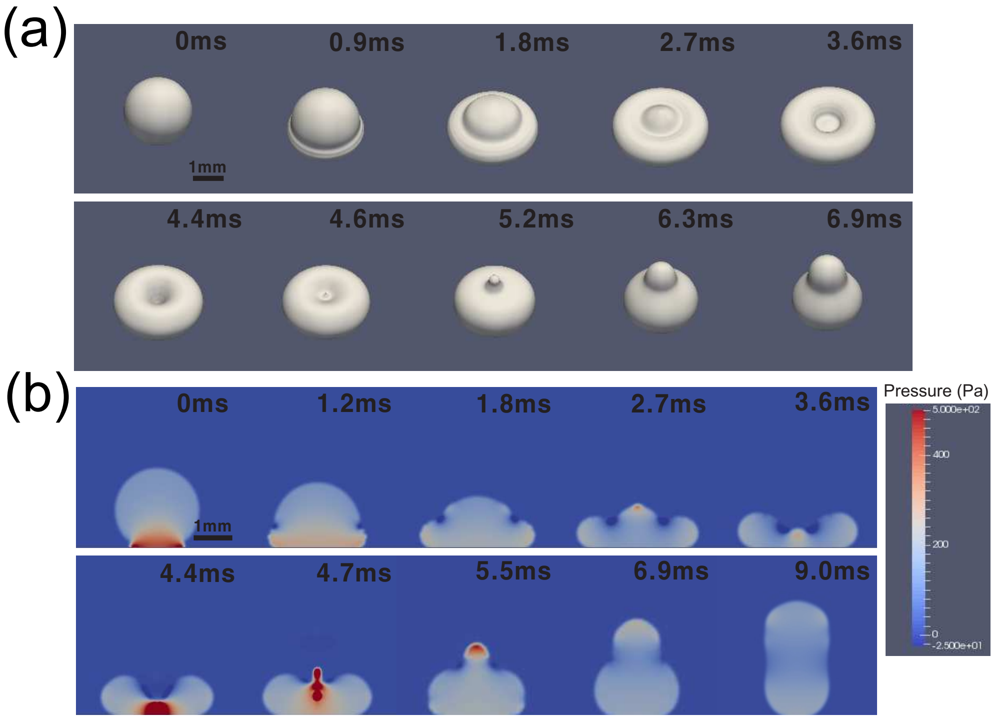

Fig. 5 (a) Numerically simulated drop impact dynamics at U=0.4 m/s. (b) Pressure contour inside the water drop during drop impact.

vicinity during the drop impact: close after the initial contact and much latter on when the drop recoils from the surface (i.e., right before the jet formation in the middle). These two pressure peaks indeed precisely match the instants of occurrence of the two types of CWT observed in the experiment.

To rationalize the different threshold velocities found for the type 2 CWTs, we start with the more classical type 1 transition at early stages after contact. The build-up pressure peak results from the vertical momentum change during the typical falling-to-spreading inertial time scale $\tau_i = R_0/U$. This is simply expressed by $P_d\mathcal{A} \sim \rho\mathcal{V}U/\tau_i$, with $\mathcal{V} \propto R_0^3$ the drop volume and $\mathcal{A} \propto {R_0}^2$ the typical contact area. This yields the well-known dynamic pressure upon impact $P_d \sim \rho U^2$. As previously reported[14,33], type 1 CWT threshold is therefore attributed to a balance between $P_d \sim \rho U^2$ and $P_c = -\frac{2\sqrt{\pi\phi_s}\gamma\cos\theta_a}{L(1-\phi_s)}$. In Fig. 4b, using the pre-factor of 1.7 in front of P_d expression from previous numerical results[34], we have re-plotted the wetting transition phase diagram as a function of the impact velocity and surface capillary pressure. Indeed, the upper type 1 CWT towards a high velocity wetted surface is *quantitatively* captured by the above wetting criteria. Comparing to previous data, a similar geometric dependency upon surface structure is found in Bartolo *et al.*[14], but the critical wetting pressures are systematically lower than those reported here; a discrepancy presumably associated with less accurate definition of the surface structure made of PDMS. Note that the expression of the critical capillary pressure might take a different form for shorter pillars as demonstrated[14,33] with an associated H/L^2 dependancy. With $H = L$ our present study is safely in the infinite-height limit[14].

We now focus on the origin of type 2 CWT which is found to happen for the less robust surfaces (low P_c), at velocities lower than required for type 1 transition. Recently, a different CWT mechanism (*i.e.* different from type 1 CWT) has been reported in the literature, associated to a water hammer pressure[35,36]. The latter is expressed as $P_{wh} = k_1\rho UC$, with C is the sound velocity in water (1480 $\mathrm{m/sec}$) and k_1 is a proportionality constant. This wetting transition was observed when a water drop was gently deposited onto the surface ($U \lesssim 0.1\,\mathrm{m/s}$), and it was shown that, with a rather small proportional constant $k_1 \sim 0.001$, a reasonably good quantitative agreement could be obtained between critical capillary pressure and water hammer pressure at the transition threshold[36]. In the later study, it was suggested that the small proportional constant k_1 on the SHPo surface was due to air drainage right at the impact and k_1 would vary with geometrical patterns of the SHPo surface[37]. While such a mechanism would give a fair order of magnitude for the pressure for type 2 transition, it can be dismissed as an incorrect scenario in the present case. Indeed, while the water hammer pressure is supposed to manifest when the center of gravity of the drop reaches its minimum, we observe transition much later during the retraction stage as shown in Fig. 3. Furthermore, our numerical simulations identifies a pressure peaks which matches the temporal observation despite not accounting for liquid compressibility effect which are at the origin of water hammer pressure.

A more meaningful phenomenon in the present case could be the close temporal proximity between the upper thin liquid jet that forms and the liquid imbibition. Such a liquid jet has been reported previously[38], and associated to the singularity arising from the closure dynamics of the air protrusion that exist at the upper surface of the drop during the whole recoil phase (Fig. 5). Indeed the Rayleigh-Plesset collapse dynamics of the air cylindrical cavity generates a pressure peak which has been successfully related to the origin and dynamic properties of the jet[38]. Two elements however forbid pushing further the comparison with this mechanism. First, quantitative prediction of the maximum pressure involves the knowledge of the critical size of cavity break-up which was found to be velocity-dependent and the origin of which remained unknown. More importantly, it seems that although close, the type 2 CWT systematically manifests some time before the appearance of the jet. Concomitantly, numerical pressure fields suggest that the surface vicinal pressure – the one which matters for CWT – reaches a peak *before* the cavity collapse kicks in (Fig. 5b).

These elements led us to propose an alternative scenario accounting for the underneath pressure upon recoil. Following the approach used during the decelerating phase immediately following drop contact, we consider the vertical momentum transfer upon recoil and bouncing. While the drop rebound velocity on SHPo surfaces remains a fraction of the impact velocity U, the typical time over which the vertical velocity builds up now should be comparable with the contact time τ_c. This contact time is generally set by the natural drop oscillation period $\tau_c \sim \sqrt{\rho R_0{}^3/\gamma}$[39–41] with recent experiments yielding $\tau_c = 1.2\sqrt{\rho R_0{}^3/\gamma}$[42]. Gathering the various elements, this global argument predicts a liquid pressure set by $P_s \propto \sqrt{\rho\gamma/R_0}\,U$. As can be shown in Fig. 4b, this criteria can satisfactorily account for the type 2 CWT domain of existence, with a proportionality constant for P_s of order 1 (2.5). Moreover, the different scaling in velocity U for P_d and P_s rationalize the absence of type 2 transition at high critical capillary pressures (above 1kPa). At a fixed velocity, the dynamic pressure peak exceeds the one during recoil and is reached first during the impact scenario: the type 2 transition is therefore systematically concealed by the occurrence of type 1 imbibition. Note that here, a complete quantitative prediction could not be reached using our numerical simulations to extract the pressure pre-factor. While the qualitative agreement (precise timing of pressure peak) were independent on the various imposed surface conditions in numerical simulations, the absolute pressure peak upon recoil did show variations with the applied slip model as well as imposed contact angle. This was not the case for the initial pressure peak after contact which proved rather insensitive to surface conditions.

3.2 Wetting area

Aside from the imbibition threshold for which we just described the two different involved mechanisms, another interesting aspect of the CWT is the extent of the wetting area after the CWT occurred. This has however been hardly quantified so far, and to that purpose, we performed a separate set of experiments, limited to the type 1 CWT, high impact velocities ($U > 1$ m/s) regime, where the wetted area is captured from top view imaging. The results are summarized in Fig. 6. After the CWT, the wetted region is clearly visible, as shown in Fig. 6a, which also shows the wetted area remaining constant over time, allowing a specific wetting radius to be defined as R_w. In Fig. 6b, R_w is shown as a function of U for micropillars with five different ϕ_s (0.046, 0.081, 0.17, 0.26, 0.38) and for three different R_0 (0.85, 1.1, 1.5 mm). Our

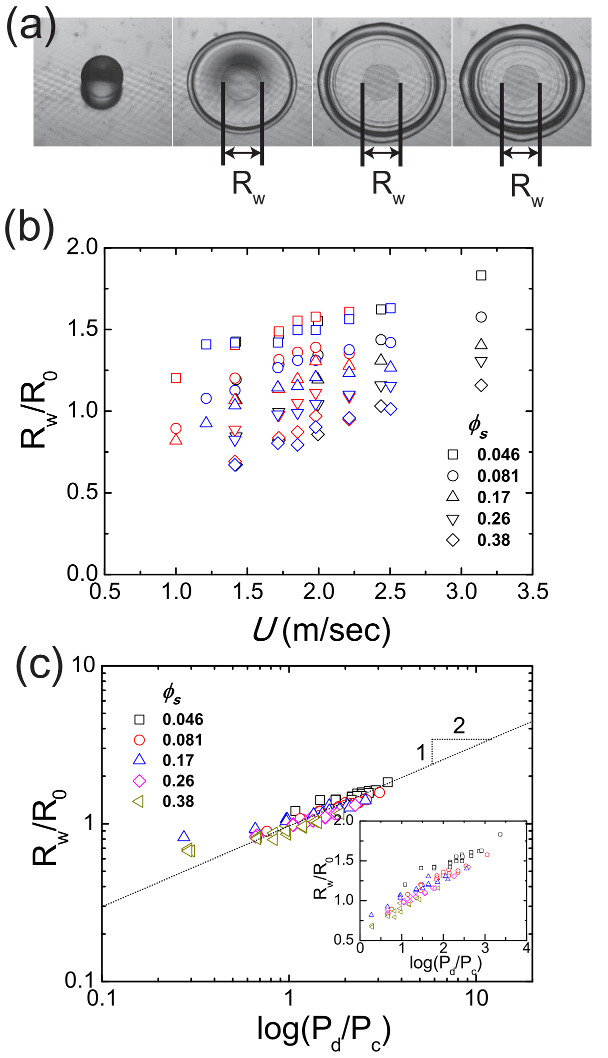

Fig. 6 (a) Wetting radius R_w on micropillars after type 1 CWT transition. (b) Nondimensionalized wetting radii as a function of an impact velocity U on microscale pillars with varying solid fractions ϕ_s for three different initial drop radius R_0 of 0.85 mm (blue), 1.1 mm (black), 1.5 mm (red). (c) Nondimensionalized wetting radii on microscale pillars as a function of the ratio of a maximum dynamic pressure P_d to a capillary pressure P_c in a log-log scale. Inset shows the same data set plotted in a linear-linear scale.

first finding is that the influence of the initial drop diameter is fully accounted for by nondimensionalizing R_w by R_0. As a rule, R_w/R_0 tends to increase as ϕ_s decreases or U increases, which corresponds, respectively, to a decrease of P_c or an increase of P_d. This trend suggests that R_w depends on a balance between P_c and P_d similarly to type 1 CWT threshold.

To rationalize this behavior, we can use a detailed numerical study of the temporal evolution of pressure field upon contact showing that right after drop impact ($t/\tau_i < 2$), the dynamic pressure $P_d(t)$ decreases exponentially over time such as $\frac{P_d(t)}{P_d(t=0)} = \exp(-1.55\frac{t}{\tau_i})$[34], where we recall that the characteristic inertial time is $\tau_i = R_0/U$. Moreover, in this early time regimes the drop shape evolution resembles a truncated sphere and the spreading radius increases with a square root of time evolution[43]. Likewise, we assumed that the contact radius R_c between the drop and the surface follows the same time dependency such as $R_c(t)/R_0 \sim \sqrt{t/\tau_i}$. Both assumptions appear to be reasonably valid in our numerical results, although our numerical results were limited to the much lower impact velocity (i.e., less than 1 m/s) due to limited computational capabilities. Neglecting spatial inhomogeneities and considering that the pressure is rather uniform at the contact area between the drop and the surface during spreading[44], R_w can be regarded as the contact radius $R_c(t)$ when the temporally decreasing dynamic pressure $P_d(t)$ becomes comparable to the capillary pressure P_c. This reasoning leads to the scaling prediction that $\frac{R_w}{R_0} \propto \sqrt{\log(\frac{P_d}{P_c})}$, suggesting that the wetted area is a function of the initial drop radius and the ratio of P_d to P_c of micropillars.

As shown in Fig. 6c, R_w/R_0 for all different microscale pillars collapse into a single master curve when plotted as a function of $\log(P_d/P_c)$, with the 1/2 slope in log-log scale agreeing with the full scaling prediction presented above. The discrepancy at the lower R_w/R_0 may be attributed to nonuniform pressure distribution at the contact region in the early times, e.g., the higher pressure at the perimeter of the contact region[45]. Our findings imply that the wetted area can be controlled through the microstructures of the SHPo surface. The ability to design the wetted area is useful for many applications such as surface patterning or ink-jet printing on SHPo surfaces where P_c is known *a priori*.

4 Conclusion

Through a series of experiments on model superhydrophobic surfaces, we revisited the Cassie-to-Wenzel wetting transition upon drop impact and showed that two distinct transitions may exist, one taking place right after contact and the other one during drop recoil prior to bouncing. Both cases were rationalized with the help of complementary numerical simulations: balancing the critical capillary pressure and peak pressures occurring within the drop, a thorough quantitative description of the imbibition phase diagram was achieved. In addition, the extent of surface spoiling associated to the remaining wetted area was experimentally characterized as a function of surface and impact parameters, and a scaling law was proposed that captures all dependencies. The present findings elucidate the complex interaction between the water drop and the SHPo surface during drop impact, allowing one to design SHPo surfaces with a specific CWT limit and wetting area for a given drop impact condition.

Acknowledgements

C.L. and J.H. thank Prof. Pirouz Kavehpour for his inspiration in initiating the project. A-L.B., C.Y., and C.P. thank ANR for funding through FREEFLOW project, contract number ANR- 11BS04-001-02, and C.L is grateful to the support from Basic Science Research Program through the National Research Foundation of Korea(NRF) funded by the Ministry of Science, ICT & Future Planning (2014R1A1A1002908). Y.N. acknowledges the support from Fundamental Technology Research Program through the National Research Foundation of Korea (NRF) funded by Korean government (MSIP) (2014M3A7B4052202)

References

1 W. Barthlott and C. Neinhuis, *Planta*, 1997, **202**, 1–8.
2 C. Lee and C.-J. Kim, *Phys. Rev. Lett.*, 2011, **106**, 014502.
3 B. Bhushan, Y. C. Jung and K. Koch, *Langmuir*, 2009, **25**, 3240–3248.
4 A. Marmur, *Biofouling*, 2006, **22**, 107–115.
5 J. Genzer and K. Efimenko, *Biofouling*, 2006, **22**, 339–360.
6 L. Mishchenko, B. Hatton, V. Bahadur, J. A. Taylor, T. Krupenkin and J. Aizenberg, *ACS Nano*, 2010, **4**, 7699–7707.
7 C. Lee, C.-H. Choi and C.-J. Kim, *Phys. Rev. Lett.*, 2008, **101**, 064501.
8 J. P. Rothstein, *Annu. Rev. Fluid Mech.*, 2010, **42**, 89–109.
9 D. Quéré, *Rep. Prog. Phys.*, 2005, **68**, 2495–2532.
10 R. J. Vrancken, H. Kusumaatmaja, K. Hermans, A. M. Prenen, O. Pierre-Louis, C. W. M. Bastiaansen and D. J. Broer, *Langmuir*, 2010, **26**, 3335–3341.
11 T. N. Krupenkin, J. A. Taylor, E. N. Wang, P. Kolodner, M. Hodes and T. R. Salamon, *Langmuir*, 2007, **23**, 9128–9133.
12 J. B. Boreyko and C.-H. Chen, *Phys. Rev. Lett.*, 2009, **103**, 174502.
13 A. Lafuma and D. Quéré, *Nat. Mater.*, 2003, **2**, 457–460.
14 D. Bartolo, F. Bouamrirene, E. Verneuil, A. Buguin, P. Silberzan and S. Moulinet, *Europhys. Lett.*, 2006, **74**, 299–305.
15 Y. C. Jung and B. Bhushan, *Langmuir*, 2008, **24**, 6262–6269.
16 M. McCarthy, K. Gerasopoulos, R. Enright, J. N. Culver, R. Ghodssi and E. N. Wang, *Appl. Phys. Lett.*, 2012, **100**, 263701.
17 D. H. Kwon and S. J. Lee, *Appl. Phys. Lett.*, 2012, **100**, 171601.
18 E. Bormashenko, R. Pogreb, G. Whyman and M. Erlich, *Langmuir*, 2007, **23**, 6501–6503.
19 G. McHale, S. Aqil, N. J. Shirtcliffe, M. I. Newton and H. Y. Erbil, *Langmuir*, 2005, **21**, 11053–11060.
20 C.-H. Choi and C.-J. Kim, *Langmuir*, 2009, **25**, 7561–7567.
21 P. Tsai, R. G. H. Lammertink, M. Wessling and D. Lohse, *Phys. Rev. Lett.*, 2010, **104**, 116102.
22 P. Papadopoulos, L. Mammen, X. Deng, D. Vollmer and H.-J. Butt, *Proc. Natl. Acad. Sci. USA*, 2013, **110**, 3254–3258.
23 M. Marengo, C. Antonini, I. V. Roisman and C. Tropea, *Curr. Op. Colloid Inter. Sci.*, 2011, **16**, 292–302.

24 R. Ramachandran, K. Sobolev and M. Nosonovsky, *Langmuir*, 2015, **31**, 1437–1444.

25 S. Shin and D. Juric, *J. Comput. Phys.*, 2002, **180**, 427–470.

26 Y. Nam, H. Kim and S. Shin, *Appl. Phys. Lett.*, 2013, **103**, 161601.

27 Y. Nam, D. Seo, C. Lee and S. Shin, *Soft Matter*, 2015, **11**, 154–160.

28 S. O. Unverdi and G. Tryggvason, *J. Comput. Phys.*, 1992, **100**, 25–37.

29 S. Osher and R. P. Fedkiw, *J. Comput. Phys.*, 2001, **169**, 463–502.

30 C. Ybert, C. Barentin, C. Cottin-Bizonne, P. Joseph and L. Bocquet, *Phys. Fluids*, 2007, **19**, 123601.

31 A. M. J. Davis and E. Lauga, *J. Fluid Mech.*, **661**, 402–411.

32 C. Cottin-Bizonne, C. Barentin and L. Bocquet, *Phys. Fluids*, 2012, **24**, 012001.

33 M. Reyssat, A. Pépin, F. Marty, Y. Chen and D. Quéré, *Europhys. Lett.*, 2006, **74**, 306–312.

34 I. V. Roisman, E. Berberovic and C. Tropea, *Phys. Fluids*, 2009, **21**, 052103.

35 T. Deng, K. K. Varanasi, M. Hsu, N. Bhate, C. Keimel, J. Stein and M. Blohm, *Appl. Phys. Lett.*, 2009, **94**, 133109.

36 H.-M. Kwon, A. T. Paxson, K. K. Varanasi and N. A. Patankar, *Phys. Rev. Lett.*, 2011, **106**, 036102.

37 S. Dash, M. T. Alt and S. V. Garimella, *Langmuir*, 2012, **28**, 9606–9615.

38 D. Bartolo, C. Josserand and D. Bonn, *Phys. Rev. Lett.*, 2006, **96**, 124501.

39 D. Richard and D. Quéré, *Europhys. Lett.*, 2000, **50**, 769–775.

40 D. Richard, C. Clanet and D. Quéré, *Nature*, 2002, **417**, 811.

41 A.-L. Biance, F. Chevy, C. Clanet, G. Lagubeau and D. Quéré, *J. Fluid Mech.*, 2006, **554**, 47–66.

42 A.-L. Biance, C. Pirat and C. Ybert, *Phys Fluids*, 2011, **23**, 022104.

43 R. Rioboo, M. Marengo and C. Tropea, *Exp. Fluids*, 2002, **33**, 112–124.

44 J. Eggers, M. A. Fontelos, C. Josserand and S. Zaleski, *Phys. Fluids*, 2010, **22**, 062101.

45 T. Maitra, M. Tiwari, C. Antonini, P. Schoch, S. Jung, P. Eberle and D. Poulikakos, *Nano Lett.*, 2014, **14**, 172–182.